Scanning X-Ray Diffraction Microscopy of a 6-GHz Surface Acoustic Wave

M. Hanke,[1,*] N. Ashurbekov,[1] E. Zatterin,[2] M.E. Msall[®],[3] J. Hellemann,[1] P.V. Santos[®],[1] T.U. Schulli,[2] and S. Ludwig[®][1,†]

[1]*Paul-Drude-Institut für Festkörperelektronik, Leibniz-Institut im Forschungsverbund Berlin e.V., Hausvogteiplatz 5-7, Berlin 10117, Germany*

[2]*ESRF, European Synchrotron, 71 Ave Martyrs, Grenoble F-38000, France*

[3]*Department of Physics and Astronomy, Bowdoin College, Brunswick, Maine 04011, USA*

Surface acoustic waves at frequencies beyond a few GHz are promising components for quantum technology applications. Applying scanning x-ray diffraction microscopy we directly map with a high lateral spatial resolution the complete strain field generated near the GaAs surface by a standing surface acoustic wave with wavelength $\lambda \simeq 500$ nm corresponding to frequencies near 6 GHz. We find that the lattice distortions perpendicular to the surface are phase shifted compared to those in propagation direction. Model calculations based on Rayleigh waves confirm our measurements. Our results represent a break through in providing a full characterization of a radio-frequency surface acoustic wave beyond plain imaging.

I. INTRODUCTION

Synchrotron-based scanning x-ray diffraction microscopy (SXDM) is a nondestructive tool to directly measure the local strain distribution of nanoscale devices [1–4] and to explore nanoscale strain dynamics operando [5,6]. In the past, it was applied to visualize and probe the time-resolved dynamics of surface acoustic waves (SAWs) at relatively long wavelengths [7–12].

SAWs, already studied in 1885 by Lord Rayleigh [13], are infamous for being the most destructive seismic waves originated by earthquakes. SAWs of much smaller wavelengths are important components of integrated circuits serving as miniature radio-frequency (rf) filters [14,15], sensors [16,17], or for microcontrolling fluids [18,19]. While these devices already in the market are based on SAWs with wavelengths beyond a few micrometers, SAWs at submicrometer wavelengths are required for alternative applications in quantum technology [20], for instance, for high-quality cavities of phonons with energies beyond approximately $10 \, \mu\text{eV}$ [21]. Such localized phonons could be used as coherent on-chip interconnects between quantum bits or as components of hybrid quantum bits [22,23].

Methods often used to characterize SAWs at lower frequencies include electrical rf reflection or transmission measurements [21], laser interferometry [24], or atomic force microscopy [25]. For high-frequency SAWs with submicrometer wavelengths, the electrical measurements suffer from impedance matching problems and the typically small amplitudes of high-frequency SAWs. While laser interferometry has an insufficient lateral resolution [24] at wavelengths well below $\lambda < 1 \, \mu\text{m}$, atomic force microscopy, in principle, has the necessary lateral and vertical resolution needed for imaging rf standing SAW (SSAW) modes. However, none of the above methods can provide a full characterization of a SAW. In contrast, SXDM can not resolve only rf SSAWs but is sensitive to all components of the three-dimensional local strain field, the essence of a SAW.

At the ID01 beamline of the European Synchrotron Radiation Facility (ESRF) [4,26–28], we perform SXDM measurements mapping the local strain field of a SSAW realized on a GaAs wafer at a phonon wavelength of $\lambda \simeq 500$ nm corresponding to a frequency near $f = 6$ GHz. Comparing our findings with the theory of Rayleigh waves [13,23] we demonstrate a remarkable agreement between the measured lattice distortions and theory predictions, which includes a characteristic phase shift between the longitudinal versus transversal SAW components.

II. SETUP AND EXPERIMENTAL TECHNIQUES

Our SSAWs are confined in acoustic microcavities aligned along the $\langle 110 \rangle$ direction on a GaAs (001) surface. The cavities, designed for quantum applications based on the coherent interaction between electrons and phonons [23], are shaped by two mirror-symmetric focusing interdigital transducers (IDTs), cf. Fig. 1(a) [20,24]. To generate a SSAW, we modulate the right-hand-side IDT gates

---

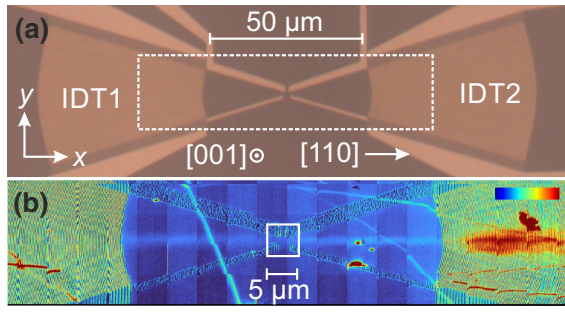*hanke@pdi-berlin.de

†ludwig@pdi-berlin.de

FIG. 1. (a) Optical micrograph of the SAW cavity consisting of two focusing IDTs with a pitch of 250 nm (not resolved) and additional guard gates in the center. The Ti/Al/Ti (10/30/ 10 nm) gates (including the IDTs), which are fabricated by electron-beam lithography, are depicted by a lighter tone on the GaAs surface with a darker color. (b) The color scale depicts, within the highlighted rectangular region in (a), the diffusely scattered intensity of the symmetric GaAs(004) reflection of a SXDM measurement. Dark-blue corresponds to the intensity of the unstrained crystal, red depicts enhanced intensity due to strain. The data are assembled of successively measured individual scans within apparent 5×5 μm^2 squares. The scanning sequence of these squares (up $\rightarrow$ down $\rightarrow$ up . . .) yields a superimposed imaging artefact of vertical stripes. The metal gates including the IDTs are clearly visible. A rf excitation of IDT2 at 5.690 GHz causes lattice distortions in the GaAs substrate underneath (red), which excites a SSAW inside the cavity along $\langle 110 \rangle$ seen as a horizontal light-blue stripe.

with an electrical rf signal, while the finger gates of the left-hand-side IDT are grounded, such that it functions as a passive Bragg mirror. In Fig. 1(b) we present a typical large-scale scanning SXDM image of the cavity including a SSAW mode at $f_{SAW} = 5.690$ GHz. The color scale depicts the intensity caused by diffusive scattering collected near the GaAs(004) reflection but excluding the intensity maximum. It expresses the local strain distribution perpendicular to the surface within the GaAs crystal. (Here, the strain includes local tilts of the surface.) Evident strain patterns below the evaporated metal gates allow an easy orientation on the surface. The SSAW appears as a horizontal stripe of enhanced strain (brighter color) centered between the IDTs. The region of maximal strain (red color) below the driven IDT is the source of the excited SSAW mode. Various additional speckles and stripes of high strain point to defects near the surface. The SXDM setup is sketched in Fig. 2(a). It shows the x-y-z piezoelectric scanning stage, which in turn is fixed to a moveable hexapod serving for controlling the orientation and rough position of the sample mounted to the piezo stage. Using a Fresnel zone plate, an x-ray beam with an energy of 10.185 keV is focused onto the sample at a focal length of 20 mm, a lateral spot size of $\simeq (30$ nm$)^2$, and a primary intensity of $\simeq 5 \times 10^9$ photons per second.
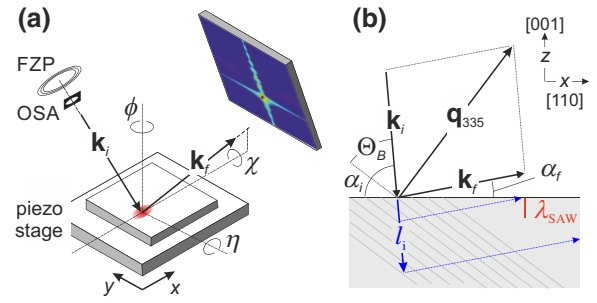

FIG. 2. Experimental setup (a) and coplanar scattering geometry (b). X-ray focusing is achieved by a combination of a 300 μm gold Fresnel zone plate (FZP) with an outermost zone width of 20 nm and an order sorting aperture (OSA). Samples are mounted on a piezo scanning stage for precise three-dimensional translations, while a hexapod on a rotation axis underneath (not shown) provides macroscopic sample translations and three orthogonal rotation axes (φ, χ, and η). The scattered intensity is recorded by a two-dimensional (2D) MAXIPIX detector. In order to maximize the spatial resolution we decided for a strongly asymmetric scattering geometry with nearly normal incidence, where l_i indicates the penetration length of the x-ray photons, cf. Appendix C.

A Rayleigh wave is expected to cause periodic crystal displacements in its propagation direction parallel to the surface, in our setup along $\langle 110 \rangle$ (x axis) and perpendicular to the surface, along $\langle 001 \rangle$ (z axis). The penetration depth of a Rayleigh wave is comparable to its wavelength, here $\lambda \simeq 500$ nm. In order to probe the related modulations of the diffraction vector $\delta \mathbf{q}$ in these two directions, we select the asymmetric (335) reflection of GaAs as $\mathbf{q}_{335}$ is composed of similar components $q_x = 4.713$ Å^{-1} and $q_z = 5.557$ Å^{-1}. The resulting diffraction geometry is co-planar, such that the scattering plane spanned by the incoming and diffracted wave vectors $\mathbf{k}_{i,f}$ is orthogonal to the crystal surface. The incidence of the x rays is for $\mathbf{q}_{335}$ almost vertical with $\alpha_i = 85.2°$, cf. Fig. 2(b). This enables a high lateral resolution near 30 nm due to a small beam footprint. It also leads to a small exit angle of $\alpha_f = 4.6°$, which causes a noticeable damping of the scattered x rays due to their path through the crystal almost parallel to the surface. This damping and the extinction depth of the incoming x rays in GaAs of $l_{ext} \simeq 4.6$ μm, both, cause a reduction of the contribution to $\delta \mathbf{q}$ as the distance to the surface, i.e., $-z$ increases.

The planar screen sketched in Fig. 2(a) shows a detector frame, which displays a reflection in reciprocal space measuring an individual spot on the surface of the fixed sample. The reflection is distorted and broadened according to the imaging function of the focused x-ray beam, including a minor contribution due to the mapping of a spherical diffraction pattern onto a planar screen. This distortion of the x-ray beam does not affect a relative shift of the reflection because of the $\delta \mathbf{q}$ caused by a SSAW.

To obtain the complete three-dimensional (3D) reflection, we measure a rocking curve by varying the Bragg angle Θ_B, cf. Fig. 2(b), by $\pm 0.2°$, which corresponds to η in Fig. 2(a). Rocking curve measurements are essential to probe different areas in reciprocal space. If using a point detector, e.g., a scintillator counter, one probes for a fixed sample and detector position just one point in reciprocal space. Here we use instead a 2D detector, which provides (again for a fixed sample and detector position) 2D information in reciprocal space. Accessing 3D data in reciprocal space requires an additional degree of freedom, realized here by rocking the sample in real space (varying η). This corresponds to a movement of the imaging plane in reciprocal space. Repeating this for different positions in the x-y plane yields a five-dimensional (5D) composite data set consisting of two dimensions in real and three in reciprocal space. It is composed of 3D images of the time-averaged intensity of the GaAs(335) reflection, while the 2D scan in real space provides its spatial variations. Applying a SSAW results in time-periodic spatial variations $\delta \mathbf{q}$ of the scattering vector, modulating the position of the reflection. Practically, the SSAW induced $\delta \mathbf{q}$ is small compared to the width of the undisturbed broadened reflection. Moreover, our measurement averages in time over many SSAW periods and we expect $\langle \delta \mathbf{q} \rangle_t \simeq 0$ for moderate SSAW powers within a linear response regime. To nevertheless analyze the effect of the SSAW, we fit the 3D scattered intensity around the GaAs(335) reciprocal lattice point (the reflection peak) with three orthogonal Gaussians and determine their individual standard deviations σ_x, σ_y, and σ_z.

III. RESULTS AND DISCUSSION

In Fig. 3(a) we present the components $\sigma_i(x,y)$ with $i = x, y, z$ for a high-resolution SXDM scan of the center of the cavity. The average values of σ_x and σ_y are similar while that of σ_z is smaller. This distortion is a consequence of the imaging function of the focused x-ray beam, see Sec. II. This leads to a distortion of the unperturbed reflection, which can be seen in the two inserts at the top of Fig. 3(a). The strong signals below the Ti/Al gates indicate distortions of the GaAs lattice, which likely occurred during cool down after the evaporation of the metals at an elevated temperature. This is an interesting observation in itself but not a topic of this paper. In addition, in the central region between the gates (highlighted by a pair of dashed lines) periodic oscillations of $\sigma_{x,z}(x)$ appear. They have a period of $\lambda/2 = 251.6$ nm and disappear if no SSAW is generated. As expected for Rayleigh waves, no such oscillations occur for σ_y.

For an analysis we model the SSAW near the center of the cavity as a superposition of a Rayleigh wave propagating in x direction and its reflection from a Bragg mirror. We consider the nonvanishing components of a Rayleigh wave, the longitudinal compression wave in x direction and the transversal shear wave in z direction. Assuming fixed ends for both relevant strain directions the SSAW is characterized by the displacement field

$$\mathbf{u}(x,z,t) = -2 \begin{pmatrix} \chi(z) \\ \zeta(z) \end{pmatrix} \begin{pmatrix} \cos(\omega t) \\ \sin(\omega t) \end{pmatrix} \sin(kx). \qquad (1)$$
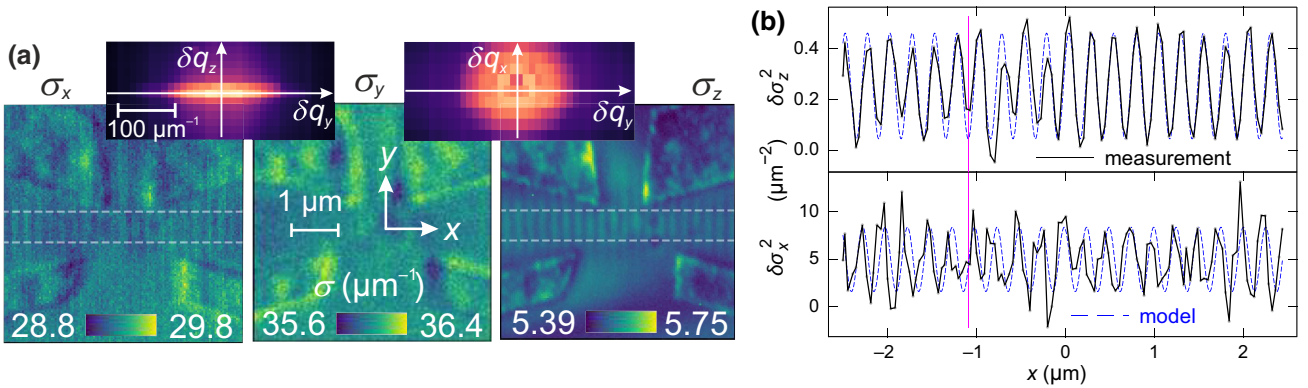

FIG. 3. (a) The upper plots show two orthogonal projections of an exemplary GaAs(335) reflection. The undisturbed widths are $(\sigma_0)_x = 29.1 \ \mu m^{-1}$ and $(\sigma_0)_z = 5.5 \ \mu m^{-1}$. The color scales of the lower plots depict the standard deviations, σ_x, σ_y, and σ_z of Gaussians fitted to the reflection along the respective directions, while we scan the center of the cavity inside the square in Fig. 1(b). In addition to the strain beneath four adjacent gates, σ_x and σ_z are enhanced along vertical stripes with the period of $\lambda/2 = 251.6$ nm, which indicate a SSAW. σ_y shows no such periodic signal. The different signal-to-noise ratios for σ_x and σ_z are related to the geometry of the resolution element in reciprocal space. (b) Contributions of the SSAW, $\delta\sigma_x^2(x)$ and $\delta\sigma_z^2(x)$, to the variances averaged along y within the regions indicated by horizontal dashed lines in (a). The solid lines are the measurements, the dashed lines (blue) are model predictions for $C = 25$ pm. The model line of σ_z is reduced by one order of magnitude. A vertical solid line facilitates the comparison of the phases between $\delta\sigma_x^2(x)$ and $\delta\sigma_z^2(x)$.

In Appendix B we discuss alternative reflection conditions. The functions $\chi(z) = 2Ce^{-\Omega_r kz}\cos(\Omega_i kz + \varphi)$ and $\zeta(z) = 2C|\gamma|e^{-\Omega_r kz}\cos(\Omega_i kz + \varphi + \theta)$ with material-dependent parameters $\Omega = \Omega_r + i\Omega_i$, $\gamma = |\gamma|e^{-i\theta}$, and $k = 2\pi/\lambda$ describe the penetration of the Rayleigh wave by about one wavelength into GaAs [23]. The constant C is proportional to the amplitude of the SSAW. A straightforward calculation based on infinitesimal strain theory, cf. Appendices A and B, yields the time-averaged modulation, $\delta\mathbf{q}$, of the diffraction vector caused by an individual scattering event as a function of x and z

$$\langle\delta q_x^2\rangle_t = 2q_x^2\left[\chi(z)k\cos(kx) + \frac{q_x}{q_z}\frac{\partial\chi(z)}{\partial z}\sin(kx)\right]^2$$

$$\langle\delta q_z^2\rangle_t = 2q_z^2\left[\frac{q_z}{q_x}\zeta(z)k\cos(kx) + \frac{\partial\zeta(z)}{\partial z}\sin(kx)\right]^2. \tag{2}$$

In Appendix D we numerically sum up the contributions of all scattered photons to the actual reflection to simulate $\sigma_{x,z}(x)$. Here we present an instructive and simplifying approximation, cf. Appendix C, which predicts identical results as our numerical simulation in the phases of $\sigma_{x,z}$ and the ratio σ_x/σ_z while the prefactor C differs by $<10\%$. The SSAW causes an additional local broadening of the unperturbed reflection by a tiny amount $\sigma_{x,z}(C)/\sigma_{x,z}(0) - 1 \sim 5 \times 10^{-3}$. Such a small perturbation motivates us to apply an incoherent model of statistically independent contributions of individual scattering events to the broadening of the reflection. Then, the measured variances can be expressed as $\sigma_i^2 = (\sigma_0)_i^2 + \delta\sigma_i^2$, where $(\sigma_0)_i$ indicates the standard deviations of the unperturbed beam and $\delta\sigma_i$ the small contributions of the SSAW. Because of $\delta\sigma_i^2 \ll \sigma_i^2$ we can further express the sum of the contributions of all scattering events along the path of the incident x-ray beam as $\delta\sigma_i^2 = \sum\langle\delta q_i^2\rangle_t$.

Integration along the incident beam finally results in the model curves for the SSAW contributions, $\delta\sigma_{x,z}^2$, plotted as dashed lines in Fig. 3(b) using the amplitude $C = 25$ pm as the only fit parameter. The vertical line near $x = -1$ μm helps visualizing a phase shift between $\delta\sigma_x^2$ and $\delta\sigma_z^2$. The corresponding experimental results are presented as solid lines, where we subtracted $(\sigma_0)_i^2$ using $(\sigma_0)_x = 29.1$ μm^{-1} and $(\sigma_0)_z = 5.5$ μm^{-1} from the undisturbed reflections. It is remarkable that our model data confirm the measured phase shift. For the chosen value of C the model agrees with the observed $\delta\sigma_x$, while the measured $\delta\sigma_z$ is an order of magnitude smaller compared to the prediction. We attribute this deviation to limitations in the quantitative analysis of the amplitude of the measured $\delta\sigma_z$, related with the finite resolution of the x-ray scan, such that only a few points are detected across the narrow width $(\sigma_0)_z$ of the reflection [29]. Note, that the accuracy of the amplitude of σ_x as well as the phases of both components are not affected by these limitations, which could be avoided in

an optimized future SXDM experiment with an increased resolution in the z direction. Given the absence of fit parameters the agreement between measured and model data regarding phase shift is remarkable good.

So far we focus on the strain field of the SSAW. However, the SXDM measurements are also suited for characterizing the cavity modes. Larger area surface scans as the one shown in Fig. 1(b) give an overview of a mode's geometry. In Fig. 4(a) we present the frequency dependence, $\sigma_z(f_{\text{SAW}})$, within 5.58 GHz $\leq f_{\text{SAW}} \leq$ 5.81 GHz determined from high-resolution surface scans as in Fig. 3 in the center of the cavity. The almost equidistant maxima correspond to the cavity modes. The mode spacing of $\delta f \simeq 25$ MHz corresponds to an effective cavity length of $L_{\text{eff}} = c/2\delta f \simeq 56$ μm, which exceeds the distance between the innermost Bragg mirror fingers by 6 μm (where we use $c = \lambda f \simeq 500$ nm $\times$ 5.68 GHz $\simeq$ 2840 m/s). The strong decrease of the peak amplitude towards the highest frequency of 5.81 GHz indicates the high-frequency end of the stop band of the Bragg mirrors. The solid line is a fit of a sum of Lorentz curves with the fit parameters plotted in Fig. 4(b). The Q factor (triangles) of the cavity reaches 750, corresponding to a phonon life time of approximately 20 ns, but decreases towards the edge of the stop band. The squares indicate the approximate area below each peak, which is proportional to the energy stored in the corresponding mode. It has a maximum around $f = 5.68$ GHz. SXDM provides a direct
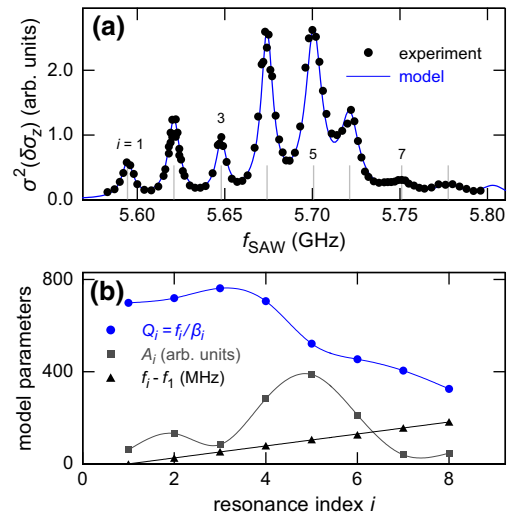

FIG. 4. (a) Variance of $\delta\sigma_z$ along line scans as shown in Fig. 3 as a function of frequency; $\sigma(\delta\sigma_z)$ is proportional to the amplitude of the SAW. The solid line is the sum of Lorentzians $\sum_i A_i\beta_i f_{\text{SAW}}/((f_{\text{SAW}}^2 - f_i^2)^2 + (\beta_i f_{\text{SAW}})^2)$. (b) Fit parameters used for the model curve in (a): quality factors $Q_i = f_i/\beta_i$ (circles), amplitudes A_i (squares), and resonance frequencies $f_i - f_1$ (triangles) as a function of the resonance index number, which we set to $i = 1$ at the lowest frequency measured cavity mode.

method for determining the true spectrum of the a rf-SAW cavity with a striking resolution.

IV. SUMMARY AND OUTLOOK

We present the first direct imaging study of the three-dimensional strain field of a rf SSAW at a frequency near 6 GHz. Even for studies of SAWs of comparable frequency, this goes far beyond what alternative methods can provide, which are at most sensitive to the displacements perpendicular to the surface. Based on our quantitative extraction of strain (with a precision of $\delta q/q \simeq 5 \times 10^{-7}$) through Bragg diffraction at the GaAs(335) reflection with a lateral resolution of 30 nm we are able to show a match of the strain field generated by the SSAW as well as its transversal and longitudinal surface displacements with the theory of Rayleigh waves. Our measurements reveal—in agreement with the model—a relative phase shift between the components of the reflection broadening along the propagation direction and perpendicular to the surface. Beyond, we demonstrate the capability of scanning x-ray diffraction microscopy to fully characterize a SSAW and its generating cavity. Our results pave the way towards alternative applications in future quantum technologies, where the complete knowledge of the three-dimensional local strain field of cavity phonons including their phases will be crucial. An example is the coupling between a coherent phonon field and a solid-state quantum bit, which sensitively depends on the local amplitude and phase of the strain-field components.

For applications in quantum technology the room-temperature characterization of a SSAW with a relatively large amplitude needs to be scaled to the few phonon regime at cryogenic temperatures. This, however, should be a straight-forward task as long as the room-temperature measurements remain within the linear-response regime regarding the SSAW amplitude. The equipment for SXDM measurements at cryogenic temperatures is in development at the ESRF.

APPENDIX A: MODULATION OF THE DIFFRACTION VECTOR BY A DISPLACEMENT FIELD

In the following we derive the modulation $\delta\mathbf{q}(x,z)$ caused by a SSAW of the scattering vector $\mathbf{q}$ of the GaAs(335) reflection used in our SXDM experiment. As in the main paper, we define the x axis to be parallel to the propagation direction [110] and the z axis to be directed in [00$\bar{1}$], which points inside the crystal perpendicular to the (001) surface. In this notation, the diffraction vector is

$$\mathbf{q} = \begin{pmatrix} q_x \\ q_z \end{pmatrix} = 2\pi \begin{pmatrix} 1/a_x \\ 1/a_z \end{pmatrix} = \frac{2\pi}{a} \begin{pmatrix} 3\sqrt{2} \\ -5 \end{pmatrix}, \qquad \text{(A1)}$$

with the lattice constant of GaAs $a = 5.6533$ Å, while $q_y = 0$. The reciprocal of $\mathbf{q}$, $\mathbf{a} = (a_x, a_z)^{\mathrm{T}} = a(\sqrt{2}/6, -1/5)^{\mathrm{T}}$, is normal to the Bragg planes and its absolute value of $\simeq 1.7$ Å is twice the distance between adjacent Bragg planes.

To determine the modulation of the diffraction vector caused by the displacement field of the SSAW we apply the concept of infinitesimal strain theory. We are interested in the variation $\delta\mathbf{q} = \mathbf{q}' - \mathbf{q}$ corresponding to a variation $\delta\mathbf{a} = \mathbf{a}' - \mathbf{a}$. In Fig. 5 we sketch the connection between the displacement vector field $\mathbf{u}$ of the SSAW and the vector $\mathbf{a}$. The displacement field shifts and tilts the Bragg planes such that $\mathbf{a} \to \mathbf{a}'$. From the sketch we can immediately see that $\delta\mathbf{u} = \mathbf{u_2} - \mathbf{u_1} = \mathbf{a}' - \mathbf{a} = \delta\mathbf{a}$.
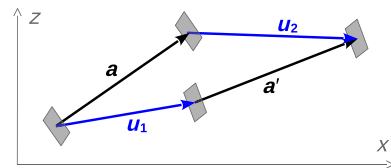

FIG. 5. Vectors $\mathbf{a}$, $\mathbf{a}'$ connecting adjacent Bragg planes, and displacements $\mathbf{u_1}$ and $\mathbf{u_2}$ of adjacent Bragg planes. The Bragg planes, which without strain are orthogonal to $\mathbf{a}$, are shifted by $\mathbf{u_1}$ and $\mathbf{u_2}$ and tilted, such that they become orthogonal to $\mathbf{a}'$.

To determine the variation $\delta\mathbf{q}$ of the diffraction vector it is convenient to start from its total differential

$$d\mathbf{q} = \frac{\partial\mathbf{q}}{\partial x}dx + \frac{\partial\mathbf{q}}{\partial z}dz. \tag{A2}$$

Assuming constant strain on the lengthscale of $|\mathbf{a}|$ (infinitesimal strain theory), we can replace $dx \to a_x$ and $dz \to a_z$ and write

$$\delta\mathbf{q} = \frac{\partial\mathbf{q}}{\partial x}a_x + \frac{\partial\mathbf{q}}{\partial z}a_z. \tag{A3}$$

Inserting the components $q_{x,z}$ from Eq. (A1) while using $\partial u_i/\partial j = \partial a_i/\partial j$ (because $\delta\mathbf{u} = \delta\mathbf{a}$) we find

$$\delta q_x = -q_x\left(u_{xx} + \frac{q_x}{q_z}u_{xz}\right)$$
$$\delta q_z = -q_z\left(u_{zz} + \frac{q_z}{q_x}u_{zx}\right), \tag{A4}$$

where we introduce the notation $u_{ij} = \partial u_i/\partial j$.

APPENDIX B: STANDING RAYLEIGH WAVES ON A GaAs WAFER

SAWs on a homogeneous crystal are Rayleigh waves, which can be described as a combination of a compression wave in the propagation direction and a shear wave perpendicular to the surface. The corresponding displacements of a Rayleigh wave can be written as

$$\mathbf{u} = \begin{pmatrix} u_x \\ u_z \end{pmatrix} = \begin{pmatrix} \chi(z)\sin(\omega t - kx) \\ -\zeta(z)\cos(\omega t - kx) \end{pmatrix}. \tag{B1}$$

For GaAs the functions $\chi(z)$ and $\zeta(z)$, which describe the penetration of the SAW into the crystal, are [23]

$$\chi = 2Ce^{-\Omega_r kz}\cos(\Omega_i kz + \varphi),$$
$$\zeta = 2C|\gamma|e^{-\Omega_r kz}\cos(\Omega_i kz + \varphi + \theta), \tag{B2}$$

with $\Omega = \Omega_r + i\Omega_i \simeq 0.5 + 0.48i$, $\gamma = |\gamma|e^{-i\theta} \simeq 1.345e^{-4.182i} = -0.68 + 1.16i$, and $\varphi \simeq 1.05$. Directly at the surface $\chi(z)$ and $\zeta(z)$ are both positive, which results in a retrograde elliptical motion of surface elements for a propagating Rayleigh wave.

A standing wave can be described as the superposition of a left-moving and a right-moving wave of equal amplitudes and frequencies, where their phase differences depend on the reflection conditions at the ends of the cavity. Since the SAW penetrates into the Bragg mirror, it is convenient to introduce an effective cavity length L_{eff}, which exceeds the distance between the innermost mirror gates L. In the main paper, we determine $L_{\text{eff}} = 56\,\mu$m from the frequency separation of the modes, which

corresponds to a penetration depth of $\delta L \equiv (L_{\text{eff}} - L)/2 \simeq 6\lambda$.

Our cavity is mirror symmetric, cf. Fig. 1(a). As a consequence, the standing wave modes of the cavity alternate in being mirror versus point symmetric (corresponding to even versus odd parity) in respect to the center of the cavity. Further, we can describe the reflection conditions in terms of open or fixed ends. For $\lambda \ll L_{\text{eff}}$, as is the case for our cavity, the mode number $2L_{\text{eff}}/\lambda$ is large and, hence, the choice of open versus fixed ends is irrelevant for the observed standing-wave modes. However, the phase difference between the two SSAW-induced strain components, e.g., $\delta\sigma_x$ versus $\delta\sigma_z$ depends on whether the two components u_x and u_z have the same or opposite parity. (In respect to the center of a mirror-symmetric cavity, u_x and u_z have identical parity for equal reflection conditions or opposite parity, if u_x and u_z have opposite reflection conditions.) This leaves us with two choices, which result in qualitatively different standing Rayleigh waves: either u_x and u_z have equal reflection conditions (both ends fixed or both ends open) or u_x and u_z have opposite reflection conditions (u_x has fixed ends and u_z open ends or vice versa).

1. SSAW with fixed ends for u_x and for u_z

In the main paper, we consider the case of equal reflection conditions, say fixed ends for both SAW components u_x and u_z. The corresponding standing wave has the form

$$\mathbf{u} = -2\begin{pmatrix} \chi(z) \\ \zeta(z) \end{pmatrix}\begin{pmatrix} \cos(\omega t) \\ \sin(\omega t) \end{pmatrix}\sin(kx). \tag{B3}$$

The strain field of the SSAW for fixed ends only described by the partial derivatives of the displacements is

$$u_{xx} = -2\chi k\cos(\omega t)\cos(kx),$$
$$u_{xz} = -2\frac{\partial\chi}{\partial z}\cos(\omega t)\sin(kx),$$
$$u_{zx} = -2\zeta k\sin(\omega t)\cos(kx),$$
$$u_{zz} = -2\frac{\partial\zeta}{\partial z}\sin(\omega t)\sin(kx). \tag{B4}$$

Inserting Eq. (B4) into Eq. (A4), we find the local variations of the diffraction vector caused by the SSAW

$$\delta q_x = 2q_x\left[\chi(z)k\cos(kx) + \frac{q_x}{q_z}\frac{\partial\chi(z)}{\partial z}\sin(kx)\right]\cos(\omega t),$$
$$\delta q_z = 2q_z\left[\frac{q_z}{q_x}\zeta(z)k\cos(kx) + \frac{\partial\zeta(z)}{\partial z}\sin(kx)\right]\sin(\omega t). \tag{B5}$$

Taking the time average of the square of Eq. (B5) yields Eq. (2) in the main paper. By inserting Eq. (B2) these

variations can be written in the explicit form

$$\delta q_x = 2q_x k \chi(z) \left[\cos(kx) \right.$$
$$\left. - \frac{q_x}{q_z} \Big(\Omega_r + \Omega_i \tan(\Omega_i kz + \phi) \Big) \sin(kx) \right] \cos(\omega t),$$

$$\delta q_z = 2q_z k \zeta(z) \left[\frac{q_z}{q_x} \cos(kx) \right.$$
$$\left. - \Big(\Omega_r + \Omega_i \tan(\Omega_i kz + \phi + \theta) \Big) \sin(kx) \right] \sin(\omega t).$$
$$\tag{B6}$$

2. SSAW with fixed ends for u_x and open ends for u_z

Next we perform the same calculation as in Appendix B 1 but assuming a standing Rayleigh wave with fixed ends for u_x and open ends for u_z. It has the form

$$\mathbf{u}(\mathbf{r}, t) = -2 \begin{pmatrix} \chi(z) \\ \zeta(z) \end{pmatrix} \begin{pmatrix} \sin(kx) \\ \cos(kx) \end{pmatrix} \cos(\omega t). \tag{B7}$$

The strain field of the SSAW is described by the partial derivatives of the displacements

$$\begin{aligned} u_{xx} &= -2\chi k \cos(\omega t) \cos(kx), \\ u_{xz} &= -2 \frac{\partial \chi}{\partial z} \cos(\omega t) \sin(kx), \\ u_{zx} &= 2\zeta k \cos(\omega t) \sin(kx), \\ u_{zz} &= -2 \frac{\partial \zeta}{\partial z} \cos(\omega t) \cos(kx). \end{aligned} \tag{B8}$$

Inserting Eq. (B8) into Eq. (A4) we find

$$\delta q_x = 2q_x \left[\chi(z)k \cos(kx) + \frac{q_x}{q_z} \frac{\partial \chi(z)}{\partial z} \sin(kx) \right] \cos(\omega t),$$

$$\delta q_z = 2q_z \left[\frac{\partial \zeta(z)}{\partial z} \cos(kx) - \frac{q_z}{q_x} \zeta(z)k \sin(kx) \right] \cos(\omega t).$$
$$\tag{B9}$$

The component δq_x is identical as for two fixed ends, while δq_z is shifted in phase, both along the x axis and in time. By inserting Eq. (B2) these variations can be written in the explicit form

$$\delta q_x = 2q_x k \chi(z) \left[\cos(kx) \right.$$
$$\left. - \frac{q_x}{q_z} \Big(\Omega_r + \Omega_i \tan(\Omega_i kz + \phi) \Big) \sin(kx) \right] \cos(\omega t),$$

$$\delta q_z = -2q_z k \zeta(z) \left[\frac{q_z}{q_x} \sin(kx) \right.$$
$$\left. + \Big(\Omega_r + \Omega_i \tan(\Omega_i kz + \phi + \theta) \Big) \cos(kx) \right] \cos(\omega t).$$
$$\tag{B10}$$

APPENDIX C: MODEL USED IN THE MAIN PAPER

In our SXDM measurements we probe the standard deviations $\sigma_{x,z}$ of the broadened reflection $\mathbf{q}$ in reciprocal space. Following the model outlined in the main paper, the contribution of the strain field of the SSAW can be expressed as $\sigma_{x,z}^2 = \langle \delta q_{x,z}^2 \rangle_t$, which can be easily calculated analytically starting from Eq. (B6) for equal reflection conditions or from Eq. (B10) for opposite reflection conditions of u_x versus u_z. Our last step is adding up all contributions to the actually measured reflection by numerically integrating along the incident beam of photons.

In GaAs, the absorption length of x rays at the energy of 10.185 keV is $l_{\text{abs}} \simeq 55\ \mu\text{m}$. In comparison, the extinction depth of the x-ray beam for the (335)-reflection is much smaller because of the Bragg reflection, $l_{\text{ext}} \simeq 6.6\ \mu\text{m}$. As sketched in Fig. 2(b) of the main paper, a photon of the x-ray beam penetrates into the crystal until it is randomly scattered at a penetration length $l_i = z/\sin\alpha_i \simeq 1.004z$. Then the photon travels for the distance $l_o = z/\sin\alpha_f \simeq 12.5z$ before it leaves the crystal. For such a diffraction process at a given depth $z(l_i)$ below the surface the effects of extinction and absorption can be combined in a damping factor

$$\beta(z) = e^{-[l_i/l_{\text{ext}} + (l_i + l_o)/l_{\text{abs}}]}. \tag{C1}$$

For our $\lambda \simeq 500$ nm we find $\beta(z) \simeq e^{-0.2z/\lambda}$. The contribution of a diffraction at $z = 500$ nm to the reflection is therefore reduced by approximately 18%. The SSAW itself decays much faster, namely within one wavelength below the surface, according to $\chi(\lambda)/\chi(0) \simeq -0.05$ and $\zeta(\lambda)/\zeta(0) \simeq 0.1$. To simulate our experiment we integrate $\langle \delta q_{x,z}^2(x_z, z) \rangle_t$ along the incident beam trajectory. This integration is particularly relevant because of the oscillating behavior of $\chi(z)$ and $\zeta(z)$ for $z \leq \lambda$. Using $x_z = x(z = 0) + z/\tan\alpha_i \simeq x(z = 0) + 0.084z$ and including the depth-dependent attenuation we arrive at our prediction for the contribution of the SSAW to the shape of the reflection

$$\delta\sigma_{x,z}^2 = \frac{\int_0^\infty dz \, \langle \delta q_{x,z}^2(x_z, z) \rangle_t \, \beta(z)}{\int_0^\infty dz \, \beta(z)}. \tag{C2}$$

To determine the model curves in Fig. 3(d) we compute this integral numerically inserting $\delta q_{x,z}$ from Eq. (B6), which applies for equal reflection conditions of both components of the SSAW.
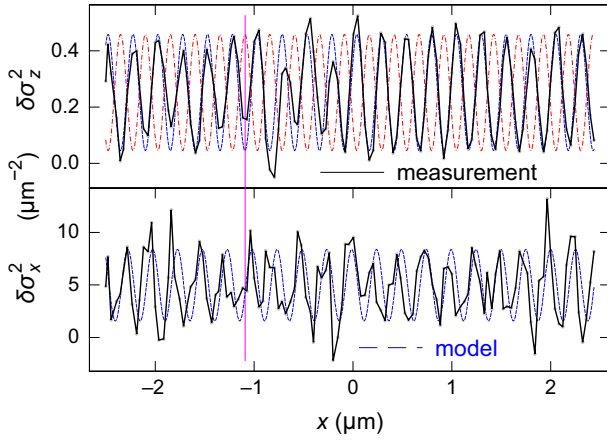
FIG. 6. Identical measured data as in Fig. 3(d) of the main paper (solid lines, black). Dashed lines (blue) are model curves for fixed ends for both SSAW components, as in Fig. 3(d) of the main paper. The dot-dashed line (red) is the corresponding model curve but using open ends for the z component of the SSAW. Its phase is shifted by π compared to the case of fixed ends. Model lines of σ_z are reduced by a factor 10.

By applying Eq. (C2) we incoherently add up the contributions to the Bragg reflections of infinitesimal volume elements along the incident x-ray beam. This incoherent approach might be questioned, as the penetration depth of the SSAW and the nominal longitudinal x-ray coherence length of about 800 nm [4] are similar. However, the photon coherence is much more reduced by the lateral focusing of the x-ray beam, which by orders of magnitude dominates the broadening of the reflections and, thus, justifies our incoherent model.

In Fig. 6 we compare the two cases of equal versus different reflection conditions of the x and z components of the SSAW, by insertion of Eq. (B6) versus Eq. (B10) into Eq. (C2). Because we vary the reflection condition for the z component of the SAW while keeping it unchanged for the x component, we find two model curves for $\delta\sigma_z^2$ with opposite phase but only one model curve for $\delta\sigma_x^2$. Note, that the phase relation between the components is fixed while we choose the overall phase for best agreement with the measured data (solid lines). Our measured data are clearly better described by the combination of equal reflection conditions, e.g., both ends fixed.

APPENDIX D: NUMERICAL SIMULATION OF THE SXDM EXPERIMENT

We test our model described above by comparing its results to numerical simulations of the SXDM experiment. Experimentally we find, that the projections of the unperturbed three-dimensional reflection to the q_x, q_y, and q_z axes of reciprocal space are well described by Gaussian distributions $\propto e^{-(q_i/2(\sigma_0)_i)^2}$. The displacement field of the SSAW causes variations of $\mathbf{q}(x,z)$. Hence, the

reflections of individual scattering events correspond to Gaussian reflections of the same shape but slightly shifted according to

$$A_i(x,z,t) \propto \beta(z)e^{-((q_i-\delta q_i(x,z,t))/2(\sigma_0)_i)^2}, \quad \text{(D1)}$$

where $\delta q_i(x,z,t)$ has to be inserted from Eq. (B6) or Eq. (B10), depending on the reflection conditions and $\beta(z)$ is the damping factor introduced in Eq. (C1) above.

Following the actual experiment, we next determine the shape of the actual reflection by numerically integrating over z (along the incident beam) and then over time

$$\alpha_i(z) \propto \int_{t=0}^{2\pi/\omega} dt \int_{z=0}^{\infty} dz A_i(x,z,t). \quad \text{(D2)}$$

Finally, we numerically determine the variances σ_i^2 and, for a direct comparison with our approximate model above, $\delta\sigma_i^2 = \sigma_i^2 - (\sigma_0)_i^2$. The numerical results resemble our approximate model results one to one in the phase difference between σ_x^2 and σ_z^2 and the ratio σ_x/σ_z, while the prefactor C differs by $<10\%$. This good agreement between the direct numerical calculation and our analytical approximation is expected, because of the small modifications of the undistorted reflection by the displacement field of the SSAW.

APPENDIX E: DISPLACEMENT AMPLITUDES OF THE SSAW—CLASSICAL REGIME

The displacement amplitudes of the SSAW at the surface are $U_x = 2C\chi(0) \simeq 0.8C$ and $U_z = 2C|\gamma|\zeta(0) \simeq 1.75C$, cf. Eq. (1), where we use $\chi(0) \simeq 0.4$, $\zeta(0) \simeq 0.65$ and $|\gamma| \simeq 1.345$. Fitting our model described above to our measurements presented in Fig. 3 we find $C \simeq 25$ pm, corresponding to displacement amplitudes at the surface of $U_x \simeq 20$ pm and $U_z \simeq 44$ pm.

From our measurements presented in Figs. 1(b) and 3 we can estimate the mode area as $A \simeq 56$ μm^2. This allows us to further estimate the displacement that a single phonon captured inside the cavity would cause, $C_0 = \sqrt{\hbar f \lambda/HA}$, where the material constant $H = 28.2 \times 10^{10}$ N/m^2 for GaAs [23]. Using $\lambda = 503.2$ nm and $f \simeq 5.675$ GHz we find $C_0 \simeq 0.138$ fm. With $C = \sqrt{N_{ph}}C_0$ we can finally estimate the number of phonons contributing to our SSAW, which is $N_{ph} \sim 10^{10}$. This large number of phonons clarifies that our measurements are probing the classical regime of SSAWs.

The resolution limit of our method makes such a large amplitude necessary. Another limiting factor is the small energy of our resonant phonons, which is about 3 orders of magnitude smaller compared to that of the dominant room-temperature thermal phonons. Nevertheless, as long as the measured SSAW is not distorted by nonlinear effects, we

expect that the SSAW of a single phonon corresponds to our measurements but scaled down to the amplitude C_0.

———

[1] M. Dubslaff, M. Hanke, M. Burghammer, S. Schöder, R. Hoppe, C. G. Schroer, Y. I. Mazur, Z. M. Wang, J. H. Lee, and G. J. Salamo, In(Ga)As/GaAs(001) quantum dot molecules probed by nanofocus high resolution x-ray diffraction with 100 nm resolution, Appl. Phys. Lett. **98,** 213105 (2011).

[2] T. Krause, M. Hanke, L. Nicolai, Z. Cheng, M. Niehle, A. Trampert, M. Kahnt, G. Falkenberg, C. G. Schroer, J. Hartmann, H. Zhou, H.-H. Wehmann, and A. Waag, Structure and Composition of Isolated Core-Shell $(In, Ga)N/GaN$ Rods Based on Nanofocus X-Ray Diffraction and Scanning Transmission Electron Microscopy, Phys. Rev. Appl. **7,** 024033 (2017).

[3] A. Al Hassan, R. B. Lewis, H. Küpers, W.-H. Lin, D. Bahrami, T. Krause, D. Salomon, A. Tahraoui, M. Hanke, L. Geelhaar, and U. Pietsch, Determination of indium content of GaAs/(In,Ga)As/(GaAs) core-shell(-shell) nanowires by x-ray diffraction and nano x-ray fluorescence, Phys. Rev. Mater. **2,** 014604 (2018).

[4] S. J. Leake, G. A. Chahine, H. Djazouli, T. Zhou, C. Richter, J. Hilhorst, L. Petit, M.-I. Richard, C. Morawe, R. Barrett, L. Zhang, R. A. Homs-Regojo, V. Favre-Nicolin, P. Boesecke, and T. U. Schülli, The Nanodiffraction beamline ID01/ESRF: A microscope for imaging strain and structure, J. Synchrotron Rad. **26,** 571 (2019).

[5] M. Abuin, Y. Y. Kim, H. Runge, S. Kulkarni, S. Maier, D. Dzhigaev, S. Lazarev, L. Gelisio, C. Seitz, M.-I. Richard, T. Zhou, V. Vonk, T. F. Keller, I. A. Vartanyants, and A. Stierle, Coherent x-ray imaging of CO-adsorption-induced structural changes in Pt nanoparticles: Implications for catalysis, ACS Appl. Nano Mater. **2,** 4818 (2019).

[6] M. Schmidbauer, M. Hanke, A. Kwasniewski, D. Braun, L. von Helden, C. Feldt, S. J. Leake, and J. Schwarzkopf, Scanning x-ray nanodiffraction from ferroelectric domains in strained $K_{0.75}Na_{0.25}NbO_3$ epitaxial films grown on (110) TbScO$_3$, J. Appl. Cryst. **50,** 519 (2017).

[7] W. Sauer, M. Streibl, T. H. Metzger, A. G. C. Haubrich, S. Manus, A. Wixforth, J. Peisl, A. Mazuelas, J. Härtwig, and J. Baruchel, X-ray imaging and diffraction from surface phonons on GaAs, Appl. Phys. Lett. **75,** 1709 (1999).

[8] E. Zolotoyabko and J. P. Quintana, Time and phase control of x-rays in stroboscopic diffraction experiments, Rev. Sci. Instrum. **73,** 1643 (2002).

[9] S. J. Whiteley, G. Wolfowicz, C. P. Anderson, A. Bourassa, H. Ma, M. Ye, G. Koolstra, K. J. Satzinger, M. V. Holt, F. J. Heremans, A. N. Cleland, D. I. Schuster, G. Galli, and D. D. Awschalom, Spin-phonon interactions in silicon carbide addressed by Gaussian acoustics, Nat. Phys. **15,** 490 (2019).

[10] D. Irzhak and D. Roshchupkin, X-ray diffraction on the x-cut of a $Ca_3TaGa_3Si_2O_{14}$ single crystal modulated by a surface acoustic wave, J. Appl. Phys. **115,** 244903 (2014).

[11] Z. Insepov, E. Emelin, O. Kononenko, D. V. Roshchupkin, K. B. Tnyshtykbayev, and K. A. Baigarin, Surface acoustic wave amplification by direct current-voltage supplied to graphene film, Appl. Phys. Lett. **106,** 023505 (2015).

[12] T. Reusch, F. Schülein, C. Bömer, M. Osterhoff, A. Beerlink, H. J. Krenner, A. Wixforth, and T. Salditt, Standing surface acoustic waves in LiNbO$_3$ studied by time resolved X-ray diffraction at PETRAIII, AIP Adv. **3,** 072127 (2013).

[13] L. Rayleigh, On waves propagated along the plane surface of an elastic solid, Proc. Lond. Math. Soc. **s1-17,** 4 (1885).

[14] C. C. W. Ruppel, Acoustic wave filter technology–a review, IEEE Trans. Ultrason. Ferroelectr. Freq. Control **64,** 1390 (2017).

[15] S. Mahon, The 5G effect on rf filter technologies, IEEE Trans. Semicond. Manuf. **30,** 494 (2017).

[16] V. Kalinin, in *2011 IEEE Int. Ultrason. Symp.* (IEEE, Orlando, 2011), p. 212.

[17] J. Devkota, P. R. Ohodnicki, and D. W. Greve, SAW sensors for chemical vapors and gases, Sensors **17,** 801 (2017).

[18] A. Wixforth, Acoustically driven programmable microfluidics for biological and chemical applications, J. Lab. Autom. **11,** 399 (2006).

[19] X. Ding, P. Li, S.-C. S. Lin, Z. S. Stratton, N. Nama, F. Guo, D. Slotcavage, X. Mao, J. Shi, F. Costanzo, and T. J. Huang, Surface acoustic wave microfluidics, Lab Chip **13,** 3626 (2013).

[20] P. Delsing, *et al.*, The 2019 surface acoustic waves roadmap, J. Phys. D: Appl. Phys. **52,** 353001 (2019).

[21] S. Büyükköse, B. Vratzov, J. van der Veen, P. V. Santos, and W. G. van der Wiel, Ultrahigh-frequency surface acoustic wave generation for acoustic charge transport in silicon, Appl. Phys. Lett. **102,** 013112 (2013).

[22] F. Forster, G. Petersen, S. Manus, P. Hänggi, D. Schuh, W. Wegscheider, S. Kohler, and S. Ludwig, Characterization of Qubit Dephasing by Landau-Zener-Stückelberg-Majorana Interferometry, Phys. Rev. Lett. **112,** 116803 (2014).

[23] M. J. A. Schuetz, E. M. Kessler, G. Giedke, L. M. K. Vandersypen, M. D. Lukin, and J. I. Cirac, Universal Quantum Transducers Based on Surface Acoustic Waves, Phys. Rev. X **5,** 031031 (2015).

[24] P. V. Santos, M. E. Msall, and S. Ludwig, *2018 IEEE Int. Ultrason. Symp.* (IEEE, Kobe, 2018), p. 1.

[25] J. Hellemann, F. Müller, M. Msall, P. V. Santos, and S. Ludwig, Determining Amplitudes of Standing Surface Acoustic Waves via Atomic Force Microscopy, Phys. Rev. Appl. **17,** 044024 (2022).

[26] G. A. Chahine, M.-I. Richard, R. A. Homs-Regojo, T. N. Tran-Caliste, D. Carbone, V. L. R. Jacques, R. Grifone, P. Boesecke, J. Katzer, I. Costina, H. Djazouli, T. Schroeder, and T. U. Schülli, Imaging of strain and lattice orientation by quick scanning x-ray microscopy combined with three-dimensional reciprocal space mapping, J. Appl. Crystallogr. **47,** 762 (2014).

[27] G. A. Chahine, M. H. Zoellner, M.-I. Richard, S. Guha, C. Reich, P. Zaumseil, G. Capellini, T. Schroeder, and T. U. Schülli, Strain and lattice orientation distribution in SiN/Ge complementary metal–oxide–semiconductor compatible light emitting microstructures by quick x-ray nanodiffraction microscopy, Appl. Phys. Lett. **106,** 071902 (2015).

[28] S. Leake, V. Favre-Nicolin, E. Zatterin, M.-I. Richard, S. Fernandez, G. Chahine, T. Zhou, P. Boesecke, H. Djazouli,

and T. Schülli, Coherent nanoscale x-ray probe for crystal interrogation at ID01 ESRF—The European Synchrotron, Mater. Des. **119**, 470 (2017).

[29] Related to the narrow width $\delta\sigma_z$ of the reflection, cf. Fig. 3(a), the Gauss curves in z directions are fitted to very few, albeit accurate, measurement points. Such a situation can result in a systematic numerical error, which, here, limits the resolution of $\delta\sigma_z^2$. The resolution might be improved in a future synchrotron campaign. The phase of $\delta\sigma_z^2(x)$ is determined from the periodic oscillation of the signal as a function of x and is much more accurate than the amplitude of this oscillation.